Aeroacoustic investigation of an oscillating airfoil in the pre- and post-stall regime

Yannick D. Mayer[a], B. Zang[a], Mahdi Azarpeyvand[a,*]

[a]*Faculty of Engineering, University of Bristol, United Kingdom*

Abstract

The present study describes an experimental investigation of the aerodynamic and aeroacoustic characteristics of a sinusoidally oscillated NACA 0012 airfoil. The experiments were conducted in an aeroacoustic wind tunnel with a uniquely designed Kevlar-walled test section. Prior to experiments, these Kevlar walls were calibrated carefully and shown to provide reliable and accurate aerodynamic and aeroacoustic measurements. Two different regimes of interest, namely the pre- and post-stall angle of attack regimes, have been examined for lift curve polars, far-field noise spectra and unsteady surface pressure spectra. Interestingly, when the lift curve polar hysteresis is small at pre-stall angles of attack, the unsteady surface pressure spectra of the oscillating airfoil can be predicted with satisfactory accuracy using a position-based weighted averaging approach from its static counterparts. On the other hand, such a method becomes invalid at post-stall angles due to the presence of a significant dynamic stall hysteresis. Instead, an increase in the mean surface pressure and far-field noise spectra is observed at dynamic stall conditions. Furthermore, a short-time Fourier transform analysis reveals that the increase of the surface pressure spectra is a direct result of the periodic production and convection of dynamic stall vortices.

Keywords: Oscillating airfoil aeroacoustics, Kevlar-walled anechoic tunnel, Dynamic stall, Unsteady surface pressure fluctuations, NACA 0012 airfoil, Trailing edge noise.

1. Introduction

The World Health Organization (WHO) has highlighted in their 2018 report that environmental noise is now Europe's second biggest environmental health threat after air pollution [2]. In most applications concerning aerodynamic noise, airfoil self-noise is a major component and contributor to environmental noise,

*Corresponding author: m.azarpeyvand@bristol.ac.uk, Queen's Building, University Walk, BS8 1TR, Bristol, United Kingdom.

A preliminary version of this paper was presented at the 2019 AIAA/CEAS Aeroacoustics Conference in Delft, The Netherlands [1].

such as helicopters and wind turbines, *etc.* The existing noise pollution can have various adverse health effects, including cardiovascular diseases, hearing impairment, tinnitus and mental health problems [2, 3]. In order to reduce the noise emissions from airfoils, various passive and active techniques are being researched and implemented, such as trailing edge serrations, porous treatments and boundary layer blowing [4–10].

In order to propose more silent airfoils, researchers and engineers utilize various techniques including aeroacoustic wind tunnel testing and computational modelling. However, at present the majority of aeroacoustic wind tunnel testing is limited to static airfoil tests, *i.e.* fixed at a specific angle of attack (AoA), while engineering machinery regularly encounters dynamically changing inflow conditions, regarding local angle of attack, turbulence intensity, *etc*, which can result in the occurrence of dynamic stall [11]. In the case of wind turbines, Smith *et al.* have hypothesized that dynamically changing wind conditions and possibly stall can cause "other amplitude modulation", described as a low frequency thumbing noise [12]. An analysis by Oerlemans also revealed that non-uniform inflow caused by wind shear, topology, large-scale turbulence, wind veer and wake operation can lead to rapidly changing AoAs and OAM for wind turbines [13], with similar conclusions also reached in other studies [14, 15]. With a practical interest, Oerlemans *et al.* also conducted field tests on a 94 m diameter wind turbine to investigate different noise reduction strategies [16]. They found that under normal operating conditions the dominant noise emission is due to the trailing edge noise from the outboard region of wind turbine blades, and that both trailing edge serrations and airfoil geometry changes could reduce the overall noise levels. In a laboratory environment, Zajamsek *et al.* conducted a study of rotating NACA 0012 airfoils for AoAs of up to $\alpha = 10\,^\circ$ and rotor tip Reynolds numbers of up to $Re_c = 240{,}000$. [17] Their investigation determined the dominant noise source to be trailing edge noise originating in the outer section of the rotor and was able to predict the noise emissions by employing a modified Brooks, Pope and Marcolini [18] airfoil self-noise model.

While the aerodynamics of pitching airfoils, in particular dynamic stall has been studied thoroughly over the years [11, 19–21], and modelled to various degrees of accuracy (see Holierhoek *et al.* [22] for an

overview), there is currently a rather limited number of aeroacoustic investigations of pitching airfoils. Nagarajan *et al.* [23] computationally studied the flow past an oscillating NACA 0012 airfoil at a Reynolds number of $Re_c = 130{,}000$ using large eddy simulation and unsteady RANS approaches, but rather few aeroacoustic results were reported. Siegel *et al.* conducted a dynamic stall experiment at a Reynolds number of $Re_c = 800{,}000$ utilizing a NACA64-618 airfoil oscillating in pitch about its quarter-chord [24]. The largest noise increase was found at the cut-off frequency of the anechoic chamber at $f = 200\,\mathrm{Hz}$. Additionally, particle image velocimetry measurements synchronized with a single microphone were used to pinpoint the flow-field locations that correlate substantially with the far-field pressure fluctuations, which were shown to correspond to the separated flow field region. A more recent experimental work by Zhou *et al.* investigated the laminar vortex shedding noise under dynamic excitation of a NACA 0012 airfoil for zero mean AoA at a low Reynolds number of $Re_c = 66{,}000$ [25]. Zhou *et al.* found a decrease in the tonal vortex shedding peak, while the broadband noise near the vortex shedding peaks was observed to increase.

By utilizing a Kevlar-walled test section that allows accurate aeroacoustic and aerodynamic investigations of dynamically oscillating airfoils, the present study aims to: (a) provide a detailed investigation on the oscillating airfoils in both pre- and post-stall regimes, including a substantial examination of the unsteady surface pressure spectra, and a comparison with the static scenarios throughout the oscillation cycle, (b) propose a position-based weighted averaging technique to estimate surface pressure spectra of oscillating airfoils using static fixed AoA spectra and examine its validity at both pre- and post-stall regimes, and finally (c) shed some light on the relationship between the flow field physics and the surface pressure statistics of dynamically stalled airfoils.

The paper is organized as follows. Section 2 provides an overview of the experimental setup, measurement techniques and the NACA 0012 airfoil. Section 3 presents the aerodynamic and acoustic characterization of the setup. Subsequently, four sinusoidally oscillating airfoil test cases with varying reduced frequencies, in the pre- and post-stall regimes, will be presented and analysed in terms of lift coefficient, far-field noise

and surface pressure spectra in section 4. The mean and time dependent surface pressure spectra discussed in section 4 are believed to be one of the first investigations of dynamic stall in terms of unsteady pressure fluctuations. Lastly, the concluding remarks are given in section 5.

2. Experimental setup

This section provides a brief description of the measurement details and the test section mounted in the aeroacoustic wind tunnel facility at the University of Bristol, including the Kevlar-walled test section, dynamic turntable, beamforming array, far-field microphone arc as well as the instrumented NACA 0012 airfoil. Kevlar-walled test sections are widely used in various anechoic wind tunnel facilities [26, 27], in order to reduce the flow deflection, while enabling far-field noise measurements. The temperature-controlled aeroacoustic wind tunnel is anechoic for frequencies above 160 Hz, and was used with a nozzle with the exit dimensions of 500 mm in width and 775 mm in height. The anechoic chamber has external dimensions of 7.9 m in length, 5.0 m in width and 4.6 m in height. Further details regarding the anechoic wind tunnel facility can be found in Mayer *et al.* [28].

2.1. Test section

An upstream and side view rendering of the test setup arrangements, aimed at enabling dynamic oscillation capabilities in an anechoic environment are illustrated in Fig. 1. A Nidec 095E3E-FM servo motor driven by a M700 Nidec servo drive with a MCi210 application module, associated SKF bearings and a zero backlash EK2 R+W coupling are mounted rigidly on two Aluminum strut stands on the sides of the Kevlar-walled test section. These far-field measurements are conducted using either a beamforming array or a microphone arc secured overhead of the test section.

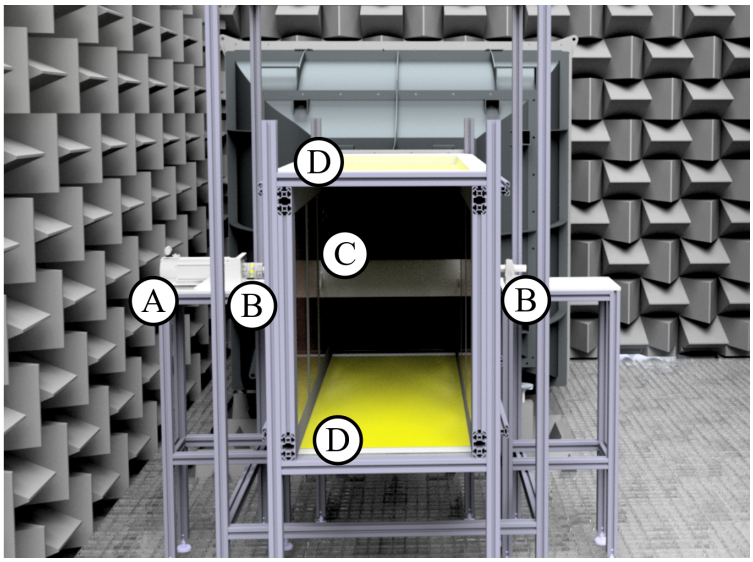

(a)

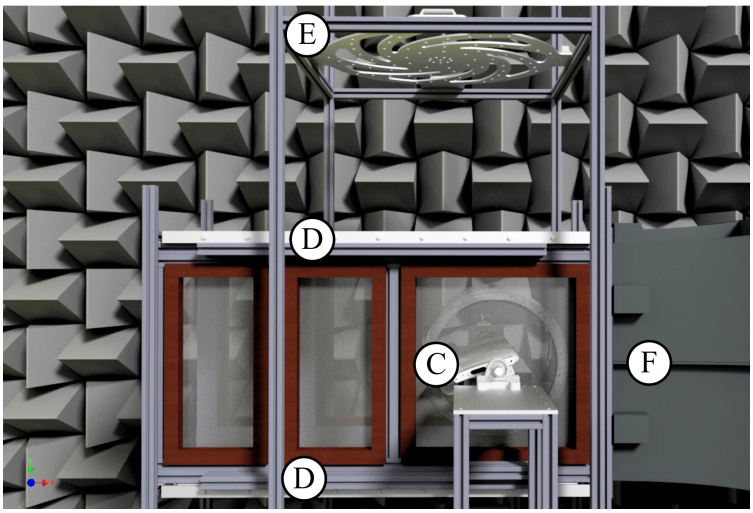

(b)

Figure 1: Schematic drawings of the experimental setup including surrounding anechoic chamber; (A) servo motor, (B) coupling and bearing, (C) NACA 0012 airfoil, (D) tensioned Kevlar cloth, (E) beamforming array and (F) nozzle: (a) upstream view and (b) side view.

The utilized servo motor and servo drive provide sufficient torque to sinusoidally oscillate the airfoil about its quarter-chord axis and to simultaneously balance any occurring moments, such as the aerodynamic pitching moment. In order to provide a smooth ramp up at the beginning of the oscillation, the sine curve

is implemented as,

$$\alpha_g(t) = \alpha_{min} + \hat{A}(1 - cos(2\pi\Omega t)), \tag{1}$$

where α_{min} denotes the minimum geometric AoA, $\hat{A}$ is the oscillation amplitude and Ω is the oscillation frequency. A mean AoA is defined as $\alpha_0 = \alpha_{min} + \hat{A}$. The maximum torque enables dynamic testing to occur up to a reduced frequency of $k_r = 0.1$ at a free stream velocity of $U_\infty = 20\,\mathrm{m\,s^{-1}}$ and a maximum amplitude of $\hat{A} = 10\,^\circ$, where the reduced frequency is defined as,

$$k_r = \frac{c\pi\Omega}{U_\infty}, \tag{2}$$

where c is the airfoil chord length. According to McCroskey [29] a reduced frequency factor of $k_r \gtrsim 0.05$ is required to achieve fully unsteady flow conditions using sinusoidal oscillations, as employed in this study. The servo motor is controlled remotely via a Modbus TCP/IP connection and the output from its internal 20 bit resolution optical encoder is recorded throughout the test duration.

The Kevlar-walled test section, as seen in Fig. 1, has a total streamwise length of 1500 mm, leaving a distance of approximately 1700 mm to the inlet plane of the anechoic chamber collector. Significant care has been taken to ensure the flow wetted areas are smooth and gap free to avoid any erroneous noise sources. At the top and bottom of the test section, bespoke tension frames are used to tension the K0120 style, plain woven Kevlar 49 fabric with a thickness of 0.12 mm. The tension in both weave directions is uniformly set to $15\,\mathrm{N\,cm^{-1}}$ and measured repeatedly using a Newman ST1E tension meter during the testing, and readjusted if necessary. The far-field noise measurements for this setup can be achieved using (a) a large beamforming array or (b) a microphone arc spanning from polar angles of $\theta = 30\,^\circ$ to $\theta = 140\,^\circ$, if the noise levels exceed the respective background noise levels. The polar angle (θ) is defined as the angle between free stream vector and the trailing edge to microphone vector, with $\theta = 90\,^\circ$ referring to the microphone vertically above the airfoil. For further details about the mechanical details and design procedures of the

whole setup, the reader is referred to Mayer *et al.* [1].

2.2. NACA 0012 airfoil

A hollow NACA 0012 airfoil with a chord length of $c = 300\,\text{mm}$ is mounted in the first window of the Kevlar-walled test section, at a distance of one chord from the nozzle exit plane. The airfoil is held in place by the servo motor and supported by two bearings. An airfoil-based coordinate system with its origin at the midspan of the leading edge is defined: x describes the chordwise direction, y the spanwise direction and z the vertical direction. Circular side plates are used to provide a smooth inner surface and the NACA 0012 airfoil is tripped at approximately $x/c = 0.1$ on both the suction and the pressure sides by means of a 6 mm wide and 0.5 mm thick zig-zag 3D turbulator trip tape by Glasfaser-Flugzeug-Service GmbH [30]. The airfoil is equipped with 87 pressure taps distributed over the airfoil, with a denser distribution of tappings near the leading edge in order to finely resolve the pressure distribution in this region. The airfoil is also fitted with unsteady pressure transducers located at the midspan, *i.e.* $y/c = 0$, in order to measure the unsteady pressure exerted on the surface of the airfoil. The majority of the unsteady pressure measurements are carried out using Knowles FG-23629-P16 condenser microphones in a direct sensing fashion, while in the trailing edge area, where little space is available, the measurements are performed in a remote sensing configuration. All microphones are placed under a pin hole of 0.4 mm diameter to avoid attenuation [31]. Moreover, all direct and remote sensing microphones were calibrated in magnitude and phase with reference to a G.R.A.S. 40PL microphone, following the procedure established by Mish [32]. The reference microphone itself was calibrated using a 42AA Pistonphone by G.R.A.S. The uncertainty of the surface pressure fluctuation measurements were determined to be 1.5 dB for a 95 % confidence interval using a Student's t-test [33]. Lastly, it is useful to note that the unsteady surface pressure fluctuation spectra of the NACA 0012 airfoil have previously been validated against experimental data by Garcia-Sagrado [1, 34].

2.3. Data acquisition and post-processing

Acoustic near- and far-field

All measurements were conducted at a set temperature of 20 °C and a free stream velocity of $U_\infty = 20\,\mathrm{m\,s^{-1}}$, which corresponds to a Reynolds number of $Re_c = \rho U_\infty c/\mu = 420{,}000$, where ρ is the air density and μ is the dynamic viscosity of air. The measurements from all unsteady surface pressure transducers were conducted simultaneously at a sampling frequency of 2^{15} Hz via five 16-channel National Instruments PXIe-4499 sound and vibration modules, mounted in a National Instruments PXIe-1062Q chassis. All data for the fixed static AoA airfoil configuration ($\Omega = 0\,\mathrm{Hz}$, $\hat{A} = 0\,°$) have been recorded for 32 s, while in the case of dynamically varied AoAs, the measurement duration was set to 50 oscillation periods ($t = 50/\Omega$). The recorded unsteady pressure transducer signals were processed in the time domain to account for the sensitivity and phase calibration curves obtained prior to the experiment. Additionally, the unsteady surface pressure measurements were corrected using the method proposed by Corcos in order to compensate for the high frequency attenuation due to the finite pin hole size [31]. Subsequently, the power spectral density (PSD) is estimated via Welch's method with a Hanning window and 50 % overlap. Frequency dependent window sizes of 2^{13}, 2^{11} and 2^8 samples are used to obtain smooth yet well-resolved spectra, resulting in frequency bin sizes of $\Delta f = 4\,\mathrm{Hz}$, 16 Hz and 128 Hz, respectively. Additionally, time dependent short-time Fourier transforms were calculated using a Hanning window with a length of 3000 samples and an overlap of 75 %, which resulted in a frequency resolution of $\Delta f = 8\,\mathrm{Hz}$ and time domain resolution of $\Delta t = 2.3 \cdot 10^{-2}\,\mathrm{s}$.

Static pressure

Two synchronized Chell MicroDaq-32 pressure scanners were used for measuring the static pressure. The data were collected at a sampling frequency of 1000 Hz and for the same sampling duration as the unsteady pressure transducers. The uncertainty of the pressure coefficient, ∂C_p, was determined following the method by Kline and McClintock [35] and was determined to be 0.064 for a free stream velocity of $U_\infty = 20\,\mathrm{m\,s^{-1}}$. The static pressure measurements are averaged for the fixed airfoil cases and phase averaged for the oscillating airfoil cases. The static pressure distributions are integrated in order to calculate the sectional lift

coefficient, C_l, and sectional pitching moment coefficient, C_m, around the airfoil quarter-chord, assuming that the surface tangential shear forces are negligible for these quantities.

Far-field beamforming array

The beamforming array is made from 73 microphones (Panasonic WM-61A) distributed along 9 arms with 8 microphones each, and an additional microphone in the center of the array, as illustrated in Fig. 2. The measurement uncertainty of the Panasonic microphones was calculated to be 1.5 dB for a 95 % confidence interval using a Student's t-test [33]. For the present study, the center of the beamforming array is aligned with the trailing edge of the NACA 0012 airfoil, at a distance of 1 m for an AoA of $\alpha = 0°$. The beamforming microphone data were recorded at a sampling frequency of 2^{14} Hz for consistent sampling durations as the unsteady pressure transducers. Subsequently, the recorded data were calibrated and the open source software package Acoular was used to calculate the functional beamforming maps [36, 37]. The spatial resolution on the rectangular beamforming evaluation grid is 2.5 mm and the cross power spectral density matrix is calculated using Welch's method using a block size of 2^{11} with a Hanning window and 50 % overlap. The vertical distance from the beamforming microphone plane to the trailing edge of the airfoil was adjusted to account for the trailing edge movement at non-zero AoAs. For the oscillating airfoil cases, the vertical distance corresponding to the mean AoA, α_0, was employed for the noise location analysis.

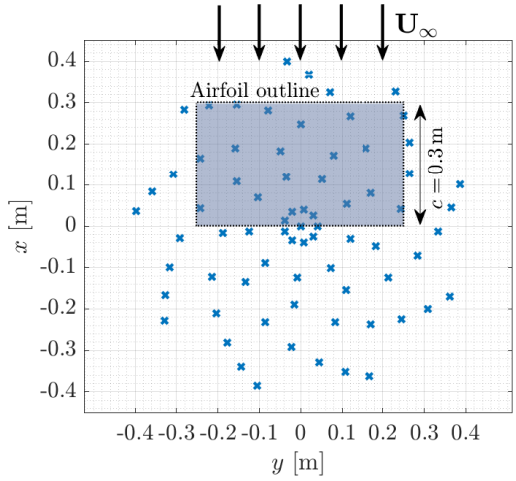

Figure 2: Beamforming geometry with 73 microphones and NACA 0012 airfoil planform at $\alpha = 0°$.

3. Kevlar wall test section characteristics

3.1. Acoustic properties

Kevlar cloth is known to cause sound attenuation, particularly at high-frequencies [38]. Hence, in order to correct the far-field noise results, the attenuation of sound waves through the tensioned Kevlar cloth needs to be quantified and later applied to the measured data. Similarly, the boundary layers developed on the inside of the Kevlar windows introduce additional noise attenuation which needs to be taken into account. The procedure to correct for these effects, established by Devenport *et al.* [39], will be followed in this paper. All acoustic tests involve a Teufel Boomster speaker, incorporating 2 tweeters, 2 mid-range drivers and a subwoofer loudspeaker placed below the test section and driven with white noise. The speaker noise was quantified to be at least 20 dB higher than any flow background noise for all frequencies greater than 160 Hz (cut-off frequency of the anechoic chamber) and all flow speeds investigated. This setup will be used to evaluate the transmission loss of (a) the Kevlar cloth and (b) the boundary layer forming on the Kevlar cloth.

Firstly, the far-field noise results at $\theta = 90\,°$ with and without the Kevlar test section without any flow

($U_\infty = 0\,\mathrm{m\,s^{-1}}$) allow the transmission loss of the Kevlar cloth, Δ_{Kevlar}, to be established in the form of

$$\Delta_{Kevlar} = 9.365 * 10^{-3}\left(\frac{f}{1000}\right)^2, \tag{3}$$

where f is the frequency. Figure 3 (a) shows a comparison between the narrowband experimental transmission loss, the quadratic data fit and the results obtained by Devenport *et al.* [39]. It can be seen that the experimentally obtained narrowband data were characterized by oscillatory behavior which is in agreement with Li *et al.* [26], Devenport *et al.* [39] and Jaeger *et al.* [38], and that the quadratic data fit is in close agreement with the quadratic data fit obtained by Devenport *et al.* [39].

Secondly, the far-field noise results of a microphone at $\theta = 90\,^\circ$ above the test section with the Kevlar windows and flow velocities of $10\,\mathrm{m\,s^{-1}}$, $20\,\mathrm{m\,s^{-1}}$ and $30\,\mathrm{m\,s^{-1}}$ are used in comparison with the no-flow results. This permits an estimate of the noise transmission attenuation due to the presence of the boundary layer on the inside of the tensioned Kevlar. Devenport *et al.* [39] established the boundary layer losses as

$$\Delta_{Bl} = \left(1 - e^{-\beta f}\right)\left(\epsilon_1 M + \epsilon_2 M^2\right), \tag{4}$$

where M is the Mach number, $\beta = 1.057 * 10^{-3}$ and ϵ_1 and ϵ_2 are empirically obtained constants. A least squares data fit resulted in $\epsilon_1 = 14.51$ and $\epsilon_2 = -0.23$. The fact that the value of ϵ_2 is two orders of magnitude below the value of ϵ_1 shows that at low velocities, the boundary layer losses scale almost linearly with the free stream velocity. Note that extra care has to be taken to divide the losses, both transmission loss, Δ_{Kevlar}, and boundary layer loss, Δ_{Bl}, by a factor of 2, as the sound field passes through two tensioned Kevlar cloths. An overview of the total far-field attenuation for flow velocities of $U_\infty = 10\,\mathrm{m\,s^{-1}}$, $20\,\mathrm{m\,s^{-1}}$ and $30\,\mathrm{m\,s^{-1}}$ is shown in Fig. 3 (b).

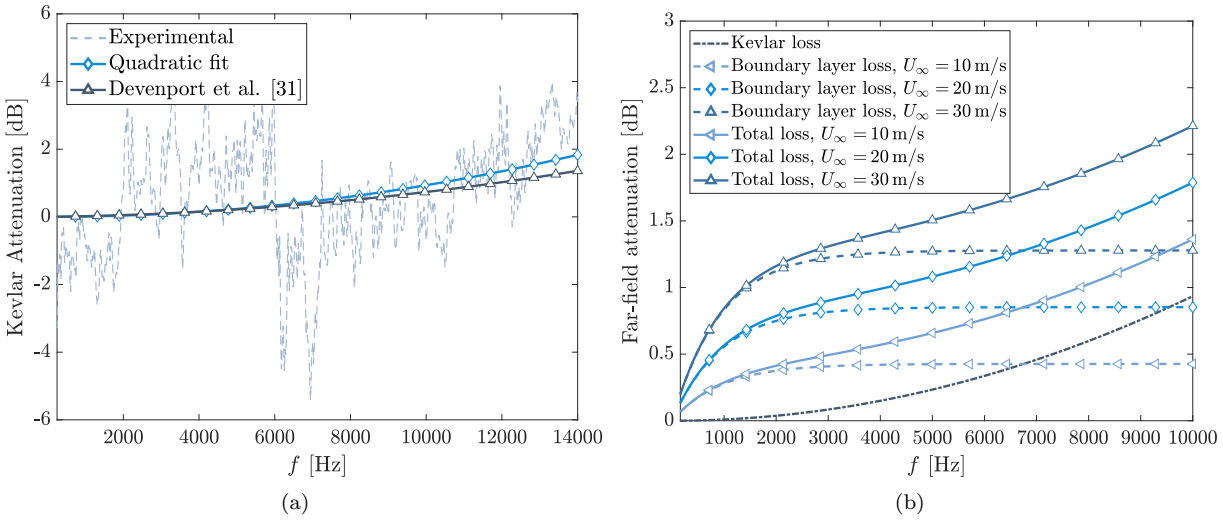

Figure 3: (a) Kevlar transmission loss and (b) combined far-field noise attenuation.

3.2. Aerodynamic properties

The majority of both open and closed test section wind tunnel test results require to be corrected for a multitude of effects, including solid blockage, wake blockage, streamline curvature and buoyancy corrections in order to obtain equivalent free air results [40]. The use of tensioned Kevlar walls also requires wind tunnel corrections. Kevlar walled test sections have several unique features and are considered to be open-closed hybrid test sections from a wind tunnel correction point of view. The permeability of the Kevlar cloth leads to the possibility of air entering and leaving the test section and the pressure difference across each Kevlar window results in varying Kevlar cloth deflections. These effects have been investigated analytically and numerically with a hybrid panel method by Devenport *et al.* [39, 41]. In this work, a model developed by Devenport *et al.* [41] to capture the change in the AoA is used, as

$$\alpha_e = \alpha_g(1 - \delta), \tag{5}$$

where α_e is the effective AoA, α_g is the geometric AoA and δ is the correction factor. The correction factor is defined as,

$$\delta = \frac{sgn(C_l)C}{\alpha_g U_\infty}\left(\frac{\rho U_\infty^2 |C_l| cA}{2\pi h}\right)^n, \tag{6}$$

where, C_l is the uncorrected lift coefficient, sgn is the signum function, $C = 0.03879$, $n = 0.5734$, $A = 1$ and h is the test section height.

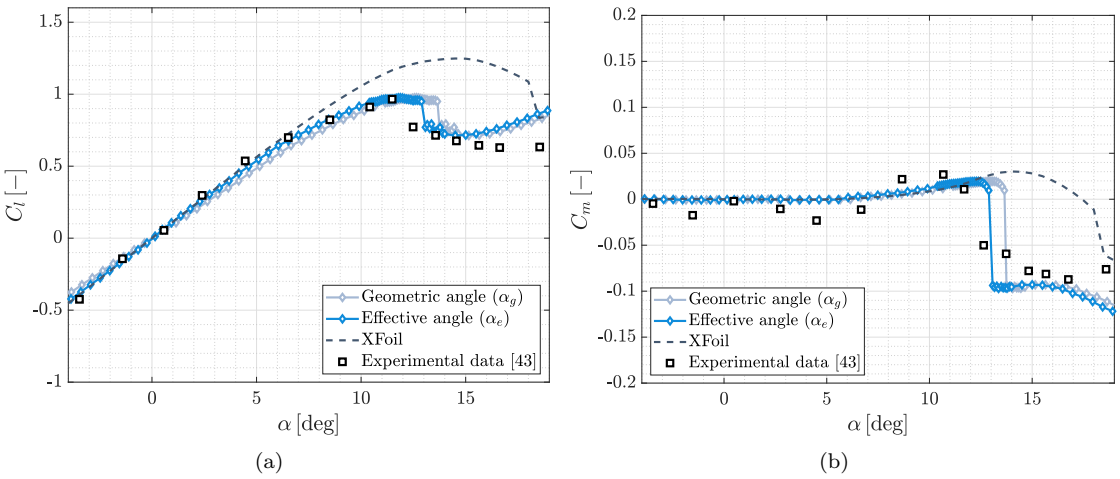

Figure 4: A comparison of the effect of the angle of attack correction, based on Eq. 5, for (a) sectional lift coefficient (C_l) and (b) sectional pitching moment coefficient (C_m).

Figure 4 shows the lift and quarter chord pitching moment coefficient polar plots for a chord-based Reynolds number of $Re_c = 420{,}000$ for varying geometric (α_g) and effective (α_e) AoAs for statically fixed airfoils. The results are also compared against viscous XFoil calculations [42] and experimental data for a NACA 0012 airfoil obtained by Sheldahl and Klimas for a Reynolds number of $Re_c = 3.6 \cdot 10^5$ [43]. It is discernible in Fig. 4 that the corrected lift coefficient and pitching moment data collapse very well with the experimental data by Sheldahl and Klimas [43], with regards to the lift curve slope in the linear AoA region, maximum lift coefficient, stall AoA and pre-stall pitching moment increase. This confirms the validity of the AoA correction method for the present experimental setup without an additional blockage correction. The lift curve slope in the linear AoA region, $|\alpha_g| < 6\,°$, also matches with the XFoil simulation results, revealing that the corrected AoA is a true free air AoA. As expected, however, XFoil overpredicts both the maximum lift coefficient, $C_{l,max}$ and maximum lift AoA, as previously noted for instance by Coder and Maughmer [44]. In the post-stall region, $|\alpha_g| > 16\,°$, the measured lift and moment coefficients start to deviate from the experimental data by Sheldahl and Klimas [43]. These small deviations in the post-stall

region could be indicative of the fact that a separation blockage correction is required to account for the separated flow region in the wake of the airfoil. However, it is believed that the blockage corrections are relatively smaller in comparison with larger facilities such as the Virginia Tech Stability tunnel, since the Kevlar cloth dimensions are smaller and therefore deflections during operation are more limited.

4. Results and discussion

Most airfoil aeroacoustic studies are performed using static airfoils, however, aeroacoustic tests under dynamic motion are assumed to become essential when changes in the inflow conditions or the use of rotating airfoils are considered. This section will investigate the surface pressure spectra, far-field noise spectra and lift coefficient changes for four oscillating test cases, namely for $\alpha_0 = 5\,^\circ$ and $12\,^\circ$, $\hat{A} = 4\,^\circ$ as well as $\Omega = 0.5\,\text{Hz}$ and $2\,\text{Hz}$, and compare the data to those of a static airfoil at comparable mean angles of attack. This section will also explore whether the unsteady surface pressure spectra for oscillating airfoils can be deduced from fixed AoA surface pressure spectra, and hence, determine the conditions for which dynamically oscillating tests become indispensable. The airfoil oscillation frequencies of $\Omega = 0.5\,\text{Hz}$ and $2\,\text{Hz}$ correspond to the reduced frequency values of $k_r = 0.024$ and 0.094, respectively. The two dynamic test cases with $\alpha_0 = 5\,^\circ$ are representative of an airfoil operating in the pre-stall AoA regime, whereas the two dynamic test cases with $\alpha_0 = 12\,^\circ$ are representative of dynamic stall. When the airfoil was oscillated, it was observed that the deflection of the Kevlar cloth varied periodically at the oscillation frequency Ω, due to the changes in the differential pressure loading on the Kevlar cloth, but no separate movements were obvious. While the Kevlar cloth deflection was small in the case of this setup, a dedicated investigation of the unsteady loading on the Kevlar walls and any associated unsteady aerodynamic corrections is believed to be beneficial.

4.1. Lift coefficient

Figure 5 presents the static sectional lift coefficient as well as the phase-averaged sectional lift coefficient for the four chosen dynamic test cases. An upstroke and downstroke motion is characterized by an upward and downward movement of the airfoil leading edge and therefore increasing and decreasing AoAs, respectively. For a mean AoA of $\alpha_0 = 5\,^\circ$ and an amplitude of $\hat{A} = 4\,^\circ$, Fig. 5 (a) reveals that the lift coefficient of the oscillating airfoil, for $\Omega = 0.5\,\text{Hz}$ and $2.0\,\text{Hz}$, closely resembles that of the static airfoil, both during the upstroke and downstroke portions of the cycle. The higher oscillation frequency, $\Omega = 2.0\,\text{Hz}$, results in a slight lift hysteresis, as analytically predicted by Theodorsen [45], while any lift polar hysteresis is effectively absent for the $\Omega = 0.5\,\text{Hz}$ case.

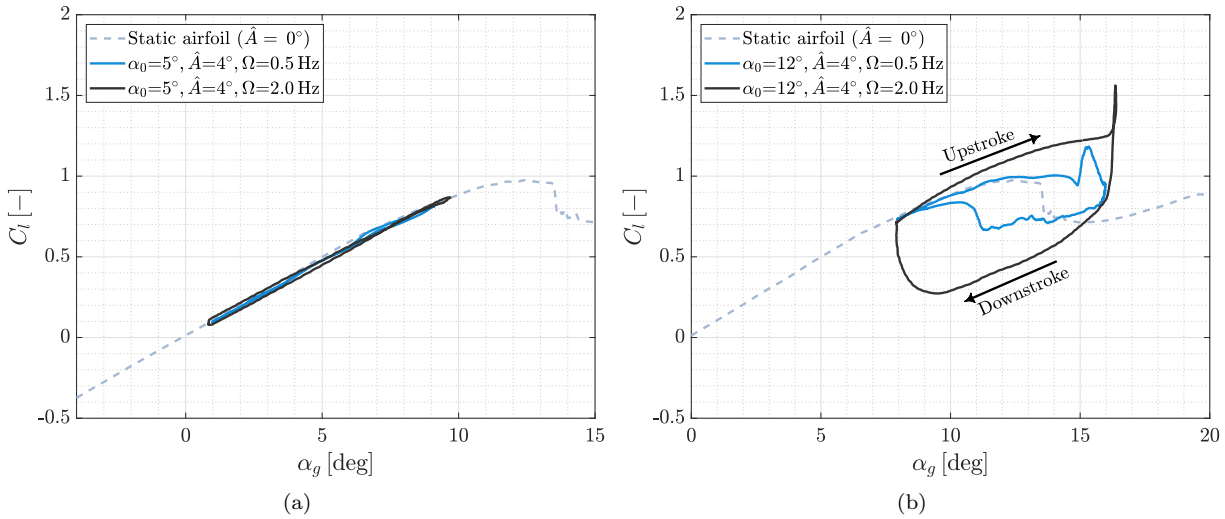

Figure 5: Mean static and phase averaged oscillating airfoil lift coefficient polar plots: (a) $\alpha_0 = 5\,^\circ$, $\hat{A} = 4\,^\circ$, $\Omega = 0.5, 2.0\,\text{Hz}$ and (b) $\alpha_0 = 12\,^\circ$, $\hat{A} = 4\,^\circ$, $\Omega = 0.5, 2.0\,\text{Hz}$.

These observations, however, change considerably for the airfoil undergoing dynamic stall ($\alpha_0 = 12\,^\circ$), where significant hysteresis is observed for both $\Omega = 0.5\,\text{Hz}$ and $2.0\,\text{Hz}$, see Fig. 5 (b). In general, during the upstroke motion the lift coefficient significantly exceeds the maximum lift coefficient of the static airfoil due to the emergence of a dynamic stall vortex and a delay in boundary layer separation due to a reduced adverse pressure gradient arising from the pitching motion around the quarter-chord [46]. The dynamic

stall vortex forms near the leading edge and results in a sudden and strong pressure decrease on the suction side of the airfoil and associated lift increases, and subsequently is convected downstream. In the following downstroke portion of the cycle, the flow reattaches, starting from the leading edge [29]. Increasing the reduced frequency of the pitch motion increases the hysteresis phenomenon, as illustrated in Fig. 5 (b), where the maximum lift coefficient observed is $C_l =$ 1, 1.2 and 1.6 for $\Omega = 0$ Hz (fixed AoA), $\Omega = 0.5$ Hz and $\Omega = 2.0$ Hz, respectively. It is also evident that for $\Omega = 2.0$ Hz, the reattachment occurs at approximately $\alpha = 8\,^\circ$, as opposed to $\alpha = 10\,^\circ$ for $\Omega = 0.5$ Hz. This delayed reattachment and the aforementioned increase in maximum lift coefficient result in a significantly larger lift curve hysteresis for $\Omega = 2.0$ Hz.

4.2. Far-field noise

While the development of appropriate noise measurement techniques for dynamic airfoils is outside the scope of the current work, the basic beamforming and direct far-field noise measurements can demonstrate the importance of the topic and provide first insights. This section investigates the noise origin from the airfoil via beamforming maps and also presents narrowband spectra for the two dynamic stall cases. Firstly, 1/3 octave band functional beamforming maps at a center frequency of $f = 1587$ Hz are presented in Fig. 6 for the static AoAs of $\alpha_g = 5\,^\circ$ and $12\,^\circ$ as well as for the two oscillating airfoil cases with $\Omega = 2.0$ Hz, $\hat{A} = 4\,^\circ$ and $\alpha_0 = 5\,^\circ$, $12\,^\circ$. It was verified that the servo motor and associated equipment noise does not exceed the background noise of the wind tunnel with the Kevlar section in place. It can clearly be seen that for all four cases the main noise sources correspond well with the trailing edge location of the airfoil, with the noise peak for $\alpha_g = 12\,^\circ$ and $\alpha_0 = 12\,^\circ$ being slightly upstream of the airfoil trailing edge planform due to the forward movement of the trailing edge at non-zero AoAs. Similar observations were made for other frequencies (not presented for brevity). The presence of trailing edge dipolar noise sources during stall was previously discussed by Moreau et al. [47]. The maximum observed noise level of 31.5 dB for the oscillating airfoil case at $\alpha_0 = 5\,^\circ$ is very much comparable to that for $\alpha_g = 5\,^\circ$, while a clear maximum noise level increase of 3 dB can be observed for the dynamic stall case, *i.e.* $\alpha_0 = 12\,^\circ$, compared to the static airfoil at $\alpha_g = 12\,^\circ$. It is crucial to note that the purpose of the functional beamforming maps is to locate the

dominant noise source and that the levels displayed are influenced by the point spread function of the array as well as the functional beamforming parameters used. Due to the width of the point spread function of the beamforming array at low frequencies and its physical size, it was not possible to distinguish the noise sources in the beamforming maps for low and medium frequencies. As will be shown in Sec. 4.3, the maxima of the surface pressure fluctuation spectra occur at frequencies of a few hundreds and a few tens of hertz for the pre- and post-stall test cases, respectively. Therefore, beamforming cannot be utilised in this case to obtain meaningful spectra including the far-field noise peaks and hence, narrowband analysis will be employed.

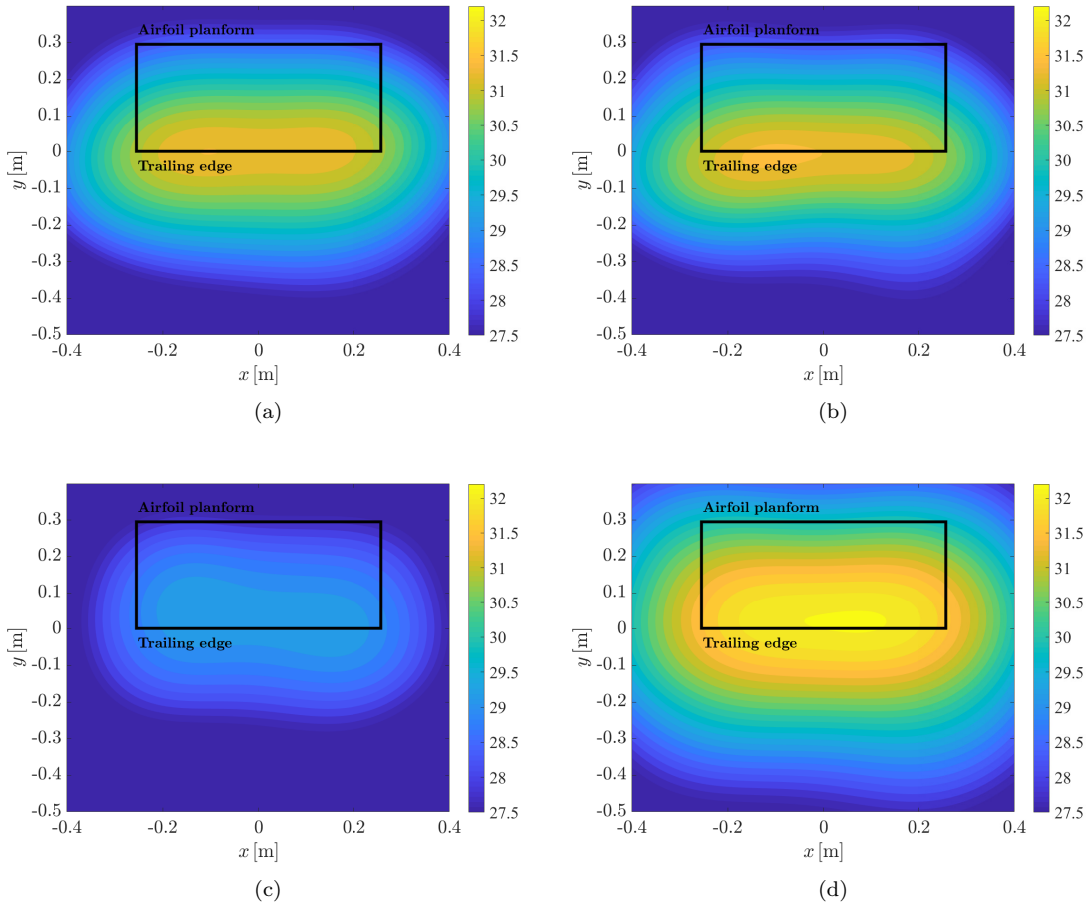

Figure 6: Corrected functional beamforming results at a center frequency of $f = 1587\,\mathrm{Hz}$ in 1/3 octave bands: (a) $\alpha_g = 5\,^\circ$, (b) $\alpha_0 = 5\,^\circ, \hat{A} = 4\,^\circ, \Omega = 2\,\mathrm{Hz}$, (c) $\alpha_g = 12\,^\circ$, (d) $\alpha_0 = 12\,^\circ, \hat{A} = 4\,^\circ, \Omega = 2\,\mathrm{Hz}$. (For interpretation of the colors in the figure, the reader is referred to the web version of this article.)

Figure 7 displays the narrowband far-field noise spectra measured directly using a microphone located

at $\theta = 90\,^\circ$, 1.75 m away from the airfoil. The corrected far-field noise spectra are presented for both the pre- and post-stall test cases. Unfortunately, due to the large nozzle height required to achieve realistic flow conditions up to high AoAs, while maintaining a low blockage, the signal-to-noise ratio is relatively low, especially for high frequencies, $f > 1000$ Hz, as observed for the far-field noise spectra when compared to the background noise spectrum. The far-field noise spectrum, for $\alpha_g = 5\,^\circ$, see Fig. 7 (a), appears to be of broadband nature and the highest noise increase is observed in the frequency range of 300 Hz to 600 Hz. As it will be shown in Sec. 4.3, this frequency range is in agreement with the highest surface pressure fluctuation levels near the trailing edge. The far-field noise spectra for the two oscillating airfoils with $\alpha_0 = 5\,^\circ$ reveal small noise increases over the static airfoil at $\alpha_g = 5\,^\circ$ for frequencies between 200 Hz to 400 Hz, while being very similar to each other.

This is in contrast with the dynamic stall far-field noise spectra displayed in Fig 7 (b), where the largest far-field noise increases are observed at the cut-off frequency of the anechoic chamber, *i.e.* $f = 160$ Hz. In agreement with previous stall noise experiments by Laratro *et al.* [48] and dynamic experiments by Siegel *et al.* [24], the stall noise spectra display a substantial low frequency noise increase, which is also observed in the surface pressure spectra shown in Sec. 4.3. The dynamic stall noise case with $\Omega = 0.5$ Hz exceeds the background noise by approximately 7 dB at $f = 160$ Hz. An increased oscillation frequency of $\Omega = 2.0$ Hz further increases the airfoil noise by 3 dB at $f = 160$ Hz. This increase is hypothesized to be a direct result of the increased hysteresis found in the lift curve polar, see Fig. 5 (b), due to a dynamic stall vortex with elevated vorticity levels. However, as it will be shown in Sec. 4.3, the main changes in the surface pressure spectra during dynamic stall occur at frequencies below the cut-off frequency of the anechoic chamber, and as a result, the presented far-field noise spectra cannot fully show the characteristics of the far-field noise spectra. As a result, no attempts have been made at present to perform short-time Fourier transform analyses, similar to those presented in Sec. 4.3 for the surface pressure fluctuations.

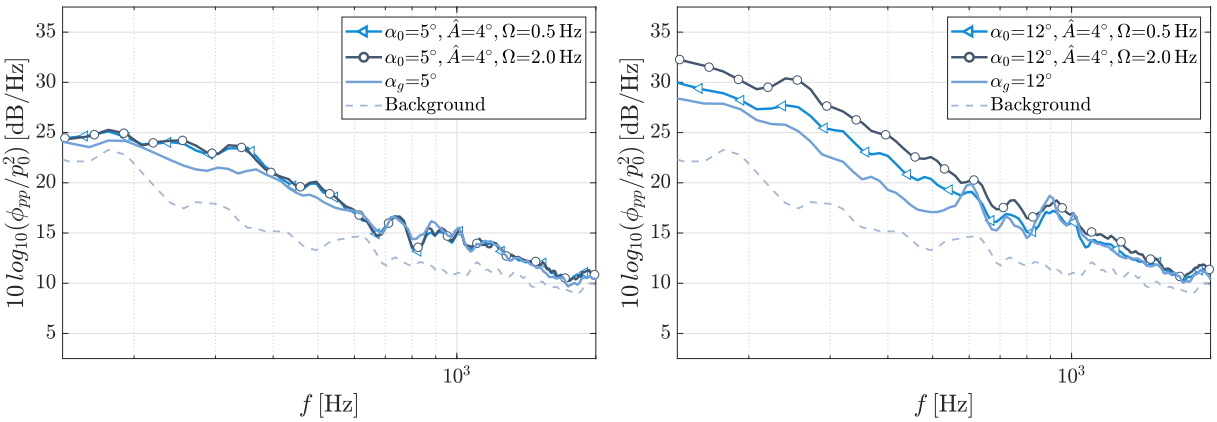

Figure 7: Narrowband far-field noise spectra: (a) $\alpha_0 = 5\,°, \hat{A} = 4\,°, \Omega = 0.5$ and 2 Hz; $\alpha_g = 5\,°$, (b) $\alpha_0 = 12\,°, \hat{A} = 4\,°, \Omega = 0.5$ and 2 Hz; $\alpha_g = 12\,°$.

4.3. Mean surface pressure fluctuation PSD spectra

A better understanding of the noise generation mechanism can be gained by studying the unsteady surface pressure spectra. According to Amiet's model [49], the far-field trailing edge noise is directly related to the surface pressure PSD and that any change in this quantity can lead to changes in the far-field noise. Moreau *et al.* also found that trailing edge dipolar noise sources are the likely fundamental noise generation mechanism for stall noise [47]. This section presents the mean unsteady surface pressure spectra results for the four dynamic test cases considered in this study and selected static AoA cases. More importantly, position-based weighted mean surface pressure spectra are calculated for the oscillating airfoil cases to provide an assessment of whether it is feasible to estimate the mean surface pressure spectra for oscillating airfoils using surface pressure fluctuation spectra from statically fixed airfoils. First of all, the weighting is performed as follows,

$$\phi_{pp}(f) = \Omega \int_0^{1/\Omega} \phi_{pp,s}\big(f, \alpha_g(t)\big)\, dt \approx \lim_{N\to\infty} \sum_{m=0}^{m=N-1} \frac{1}{N}\, \phi_{pp,s}\left(f, \frac{\alpha_g\left(\frac{m+1}{\Omega N}\right) - \alpha_g\left(\frac{m}{\Omega N}\right)}{2}\right), \tag{7}$$

where $\phi_{pp}(f)$ denotes the position weighted mean, N is an arbitrary number of segments used per oscillation cycle, $1/(N\Omega)$ is the corresponding evaluation resolution, $\phi_{pp,s}\big(f, \alpha_g\big)$ describes the fixed AoA surface pressure PSD and α_g was previously defined in Eq. 1. The angle of attack dependent fixed AoA spectra,

$\phi_{pp,s}(f, \alpha_g)$, were determined via a cubic spline interpolation from experimental measurements conducted in AoA increments of $\Delta\alpha_g = 1\,^\circ$.

All results, including those for the oscillating airfoil cases, have been obtained using Welch's power spectrum approximation and therefore present the average energy content in the surface pressure fluctuations. Figure 8 displays surface pressure spectra corresponding to the pre-stall regime, namely $\alpha_0 = 5\,^\circ$, $\hat{A} = 4\,^\circ$ and $\Omega = 0.5\,\text{Hz}$ and $2\,\text{Hz}$, as well as the fixed AoA surface pressure spectra for the mean, maximum and minimum AoAs observed during the oscillating motion, i.e. $\alpha_g = 1°$, $5°$ and $9°$. The figure illustrates that for the considered pressure transducer locations of $x/c = 0.53$, 0.73, 0.90 and 0.99, the pressure spectra levels of the dynamic test cases exceed those of the minimum and mean static AoA at low and mid frequencies by up to 5 dB, while being lower than the spectrum of the maximum AoA case. However, at high frequencies the dynamic test case spectra resemble the mean and minimum AoA spectra more closely, albeit a few decibels lower. At the same time, the dynamic spectra are substantially higher than the maximum AoA spectrum at high frequencies. The peak frequency of the oscillation test cases also corresponds to the peak frequency of the maximum AoA surface pressure spectrum.

The weighted average approximation of the oscillating cases, calculated on basis of fixed AoA pressure spectra, *i.e* Eq. 7, matches the measured spectra for the lower oscillation frequency of $\Omega = 0.5\,\text{Hz}$ very well, with a difference of less than 0.5 dB observed throughout the whole frequency range considered. Hence, the weighted average approach can be utilized to predict the surface pressure spectra of oscillating airfoils in the pre-stall regime with good degree of confidence. Fundamentally, this corroborates further the observation that the lift coefficient polar plot for $\Omega = 0.5\,\text{Hz}$ matches that of the static lift curve, see Fig. 5, indicating similar flow field characteristics. Considering the $\Omega = 2.0\,\text{Hz}$ case, it is clear that at medium to high frequencies, i.e. $f > 500\,\text{Hz}$, the pressure spectra resemble that of the oscillating case with $\Omega = 0.5\,\text{Hz}$ and therefore also matches the weighted average approximation, while surface pressure PSD increases of up to 3 dB can be observed at low frequencies. It is assumed that the shed vorticity during the dynamic motion,

which is responsible for the slight hysteresis in the lift curve, see Fig. 5, is also responsible for this increase.

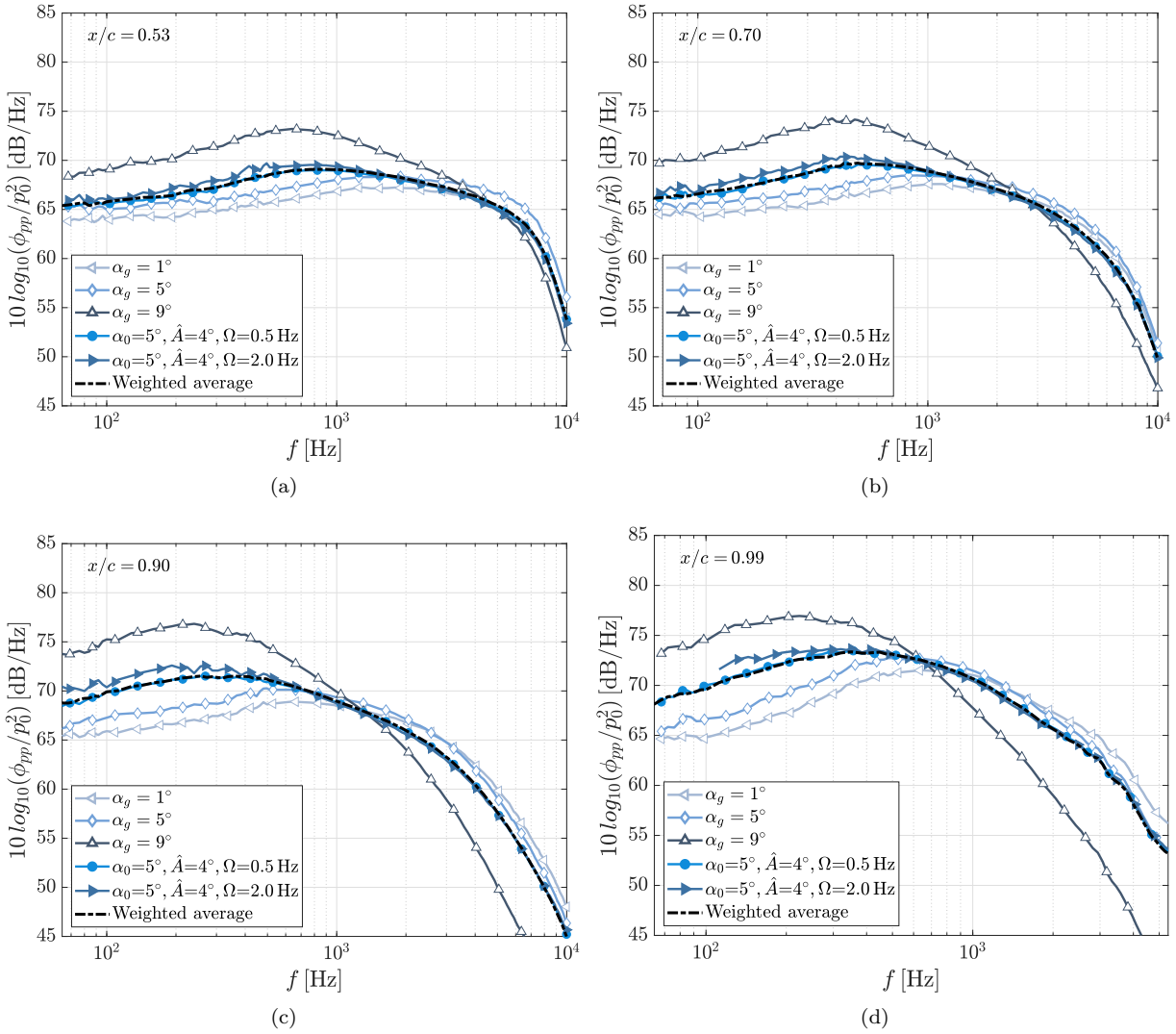

Figure 8: Surface pressure fluctuation PSD for $\alpha_g = 1°$, $\alpha_g = 5°$, $\alpha_g = 9°$, $\alpha_g(t) = 5° + 4° sin(\pi t)$ and $\alpha_g(t) = 5° + 4° sin(4\pi t)$: (a) $x/c = 0.53$, (b) $x/c = 0.70$, (c) $x/c = 0.90$ and (d) $x/c = 0.99$.

Figure 9 investigates the effects of dynamic stall on the time-averaged surface pressure spectra at the chordwise positions of $x/c = 0.53$, 0.73, 0.90 and 0.99. Results are presented for an airfoil oscillating with $\alpha_0 = 12°$, $\hat{A} = 4°$ and $\Omega = 0.5$ Hz and 2 Hz. For ease of comparison, the surface pressure spectra for the mean, maximum and minimum AoA observed during the oscillating motion, i.e. $\alpha_g = 8°$, 12° and 16° are also included. In general, the dynamic stall case with an oscillation frequency of $\Omega = 2$ Hz exceeds that of

the lower oscillation frequency of $\Omega = 0.5$ Hz by up to 4 dB for all chordwise positions and range of frequencies. For the microphone location closest to the trailing edge ($x/c = 0.99$), this difference increases further to 6 dB for frequencies of $f \leq 50$ Hz. Toward the rear of the airfoil, namely for $x/c > 0.70$, the surface pressure spectra for the $\Omega = 2$ Hz test case and $\alpha_0 = 16\,^\circ$, display a narrow peak at f =40 Hz to 44 Hz. The corresponding Strouhal numbers, $St_h = fcsin(\alpha)/U_\infty$, utilising the projected frontal height at $\alpha = 16\,^\circ$ are found to be between 0.17 to 0.18, which matches previously observed values for vortex shedding [47, 50].

In comparison to the surface pressure spectra for fixed AoAs, it is evident that for $x/c = 0.53$ and 0.7, both dynamic stall spectra on one hand follow the surface pressure spectrum of $\alpha_g = 16\,^\circ$ at low frequencies, $f < 100$ Hz, and on the other hand, the spectrum of $\alpha_g = 8\,^\circ$ for about $f > 450$ Hz, whereas exceeding all static AoA spectra for the frequency range in between. For the two chordwise pressure transducers located closer to the trailing edge, *i.e* $x/c = 0.90$ and 0.99, the dynamic stall pressure spectra follow the general trend of the surface pressure spectrum at $\alpha_g = 16\,^\circ$, with the surface pressure spectrum for $\Omega = 2.0$ Hz matching or exceeding the aforementioned static AoA spectrum. This is a marked difference to the pre-stall regime oscillation cases, where the surface pressure spectra for the oscillating airfoil cases never exceeded all presented fixed AoA surface pressure spectra. Hence, it does not come as a surprise that the weighted average spectra, based on Eq. 7, match substantially less well with the dynamic stall surface pressure spectra, than it was the case in the pre-stall regime, with deviations reaching up to 15 dB at frequencies $f < 500$ Hz. However, at higher frequencies the weighted average spectra approximate the dynamic stall spectrum for $\Omega = 0.5$ Hz very well, while underpredicting the spectrum for $\Omega = 2.0$ Hz by approximately 3 dB. This can also be explained in light of the lift coefficient polar results, shown earlier in Fig. 5 (b), revealing a substantial hysteresis for both dynamic stall cases. Since the lift coefficient for the dynamic stall cases deviates notably from the static lift curve polar, the weighted averaged approach based on static AoAs becomes less valid. The flow fields of the dynamically stalled airfoil is characterized by the dynamic stall vortex from the leading edge, which cannot be reproduced using fixed AoA airfoil testing. The results also suggest that the pitching movement and the formation of the dynamic stall vortex are more influential on the unsteady

loading at lower frequencies.

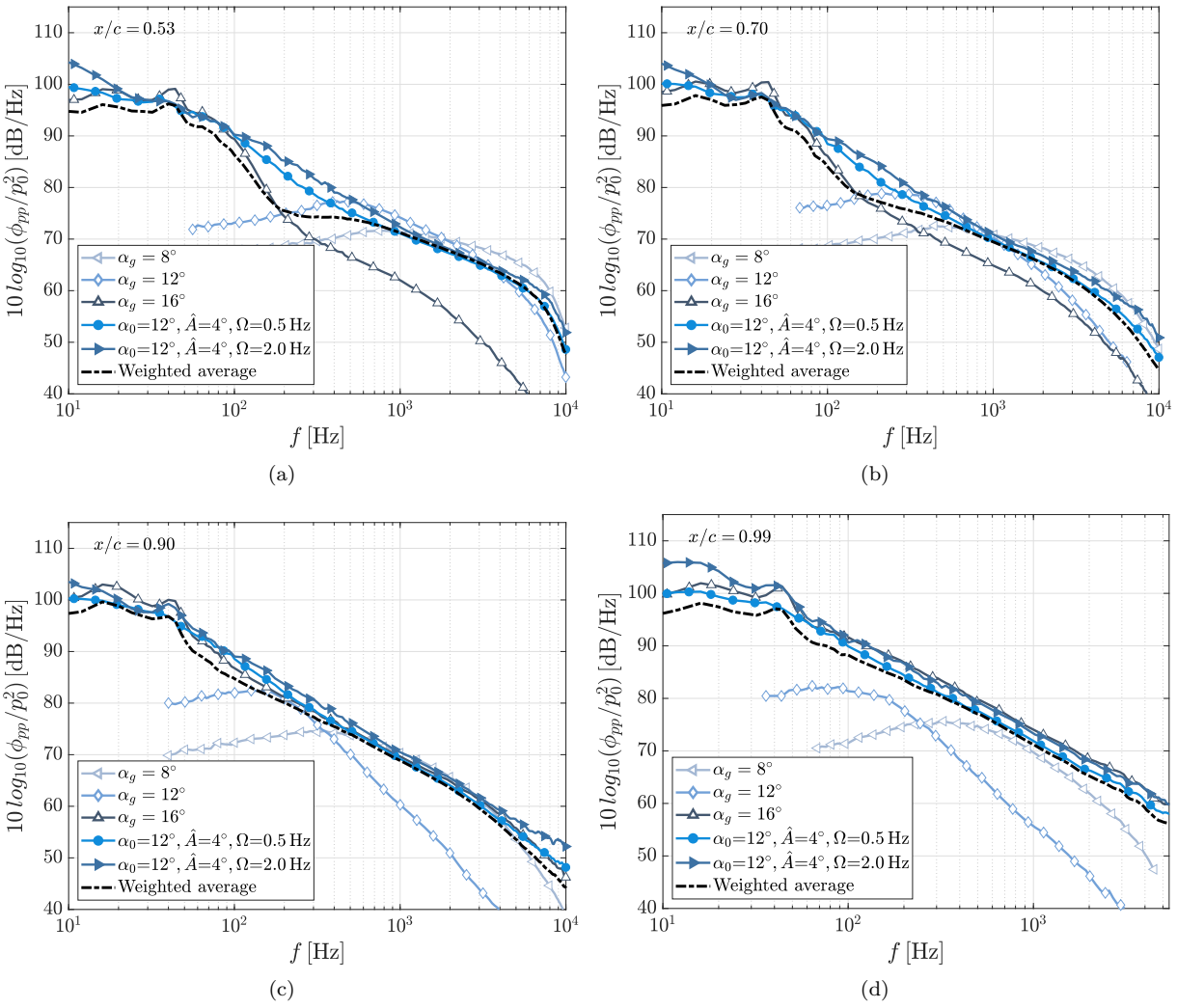

Figure 9: Surface pressure fluctuation PSD for $\alpha_g = 8°$, $\alpha_g = 12°$, $\alpha_g = 16°$, $\alpha_g(t) = 12° + 4°sin(\pi t)$ and $\alpha_g(t) = 12° + 4°sin(4\pi t)$: (a) $x/c = 0.53$, (b) $x/c = 0.70$, (c) $x/c = 0.90$ and (d) $x/c = 0.99$.

The observations in this subsection regarding the unsteady loading acting on pitching airfoils can be useful for a range of applications, such as helicopters and wind turbine blades. The results clearly indicate that one should not approximate surface pressure spectra by utilizing the static AoA surface pressure spectrum at the mean AoA, as this will result in an overprediction of the peak frequency and a substantial underprediction of the spectrum peak. Using a position weighted approximation approach, however, it is possible

to obtain an accurate estimate of the surface pressure spectrum from the fixed airfoil surface pressure PSD dataset unless dynamic stall occurs, in which case the averaged spectra can severely underpredict the low and medium frequencies. It is also worthwhile to point out that the observed spectral energy content increase for the dynamic stall cases ($\alpha_0 = 12\,^\circ$) is assumed to be at least partially responsible for the dynamic stall noise increase. Additionally, other quantities, such as the spanwise surface pressure coherence spectra are known to play an important role in noise generation mechanisms, which could lead to either an increase or a reduction of the effect of the surface pressure spectra changes.

4.4. Short-time Fourier analysis

This section investigates the time dependent energy-frequency content of the surface pressure fluctuations due to the boundary layer flow structures, measured at $x/c = 0.90$. The analysis is performed using a short-time Fourier transform (STFT) approach. All results in this section are presented for five oscillation periods, with the short-time Fourier transform results normalized by $p_0 = 20 \cdot 10^{-6}\,\mathrm{Pa}$. Additionally, each figure also contains the corresponding AoA as a function of time ($t\Omega$), for a duration of five oscillations at the bottom, while the graph on the right hand side displays the mean, maximum and minimum values of the surface pressure STFT analysis observed over 50 oscillation cycles. This analysis aims to correlate the instantaneous surface pressure spectra with flow field events as discussed in Section 4.1.

Figure 10 presents the STFT results for an airfoil set at $\alpha_0 = 5\,^\circ$, oscillating at $\Omega = 0.5\,\mathrm{Hz}$ and $2\,\mathrm{Hz}$, with an amplitude of $\hat{A} = 4\,^\circ$. The results show the surface pressure spectra variation over each oscillation period, and it is clear that low AoAs are responsible for the high frequency energy contribution, and vice versa, the higher AoAs contribute to the majority of the lower frequency energy ($f \leq 1000\,\mathrm{Hz}$). The STFT results appear to be of symmetric nature, relative to the maximum AoA during each cycle, with the maximum lower frequency ($f \leq 1000\,\mathrm{Hz}$) values occurring at the maximum AoA, and therefore indicating no surface pressure fluctuation hysteresis exists. The results also show a large variation in the energy-frequency content of the surface pressure fluctuations during each cycle, with the maximum energy level being approximately 10 dB

higher than the mean value across the whole frequency range investigated. This could give rise to temporary noise increases. Comparing Figs. 10 (a) and (b), it is noticeable that the main features are comparatively similar, which agrees well with the observation in Sec. 4.3, where only small differences between the different oscillation frequencies were observed in the spectral shape at $x/c = 0.90$.

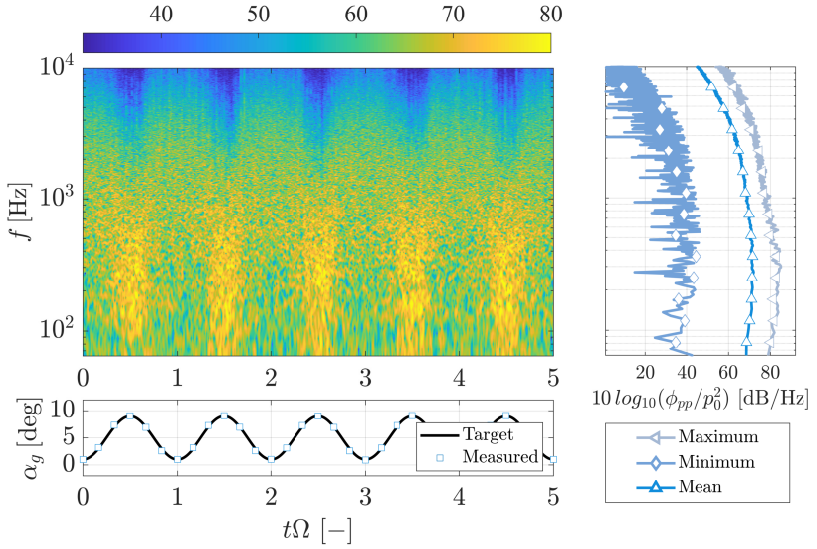

(a)

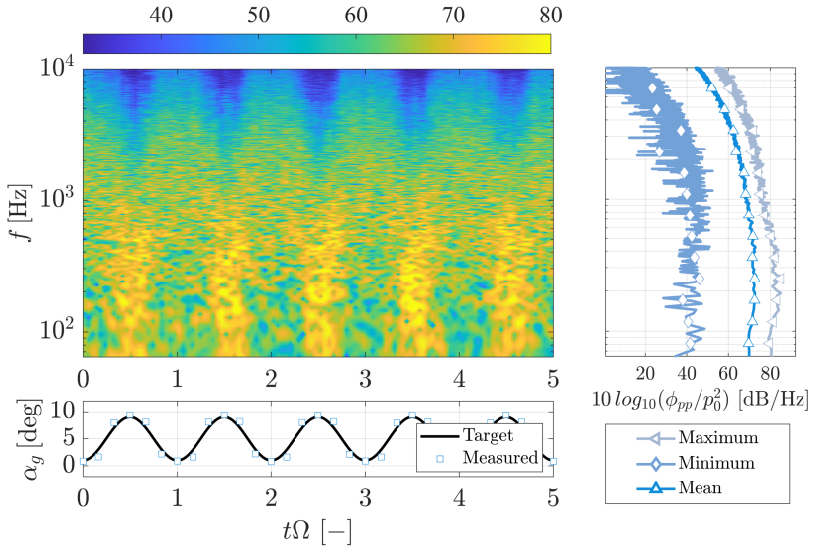

(b)

Figure 10: Surface pressure fluctuation short-time Fourier transform for five oscillation periods at $x/c = 0.90$ for $\alpha_g(t) = 5^\circ + 4^\circ sin(2\pi\Omega t)$: (a) $\Omega = 0.5$ Hz and (b) $\Omega = 2.0$ Hz.

Next, Fig. 11 presents the STFT results for an airfoil set at $\alpha_0 = 12\,^\circ$, oscillating at $\Omega = 0.5\,\text{Hz}$ and $2\,\text{Hz}$, with an amplitude of $\hat{A} = 4\,^\circ$. Unlike the STFT results for the lower mean angle of $\alpha_0 = 5\,^\circ$, the high frequency energy contribution is not limited to the low AoAs during the oscillations, but can be seen throughout each oscillation cycle, especially when flow separation takes place. As a result the STFT contour plots are no longer of symmetric nature, which indicates significant differences between the upstroke and downstroke phases of the cycle. The difference between the maximum and minimum values observed reaches values of up to 70 dB for $\alpha_0 = 12\,^\circ$ in comparison to 40 dB for $\alpha_0 = 5\,^\circ$, despite a consistent oscillation amplitude of $\hat{A} = 4\,^\circ$, revealing greater unsteadiness in the time-frequency energy content of the surface pressure fluctuations. The highest value of the surface pressure PSD at low frequencies is observed during the upstroke as well as downstroke motion for both cases at $\alpha_0 = 12\,^\circ$ and appears to be correlated with the formation of the dynamic stall vortex as well as the presence of flow separation, as deduced from Fig. 5.

Comparing the two displayed oscillation frequencies for $\alpha_0 = 12\,^\circ$ in Fig. 11, it can be seen that for $\Omega = 0.5\,\text{Hz}$, the low frequency energy content for $f \leq 20\,\text{Hz}$ decreases substantially once the flow reattaches during the downstroke phase, while this decrease is not evident for $\Omega = 2.0\,\text{Hz}$ and the energy content at very low frequencies appears virtually independent of time. This observation can also be clearly seen in the reduced difference between the minimum and maximum spectra observed for these frequencies. One can therefore conclude that the larger hysteresis, due to the higher reduced frequency, induces a relatively longer period of flow separation during each cycle, which in turn leads to a low frequency increase (also seen in Fig. 9). Another interesting observation for $\Omega = 2.0\,\text{Hz}$ is that as the dynamic stall vortex emerges during the upstroke phase, an energy burst across the entire the frequency range appears, which results in the highest surface pressure spectra values for frequencies $f > 80\,\text{Hz}$ in each cycle. This correlation between the dynamic stall vortex and the surface pressure fluctuations therefore appears to explain the increase in the higher frequency energy content for $\Omega = 2.0\,\text{Hz}$, as also seen in Fig. 9.

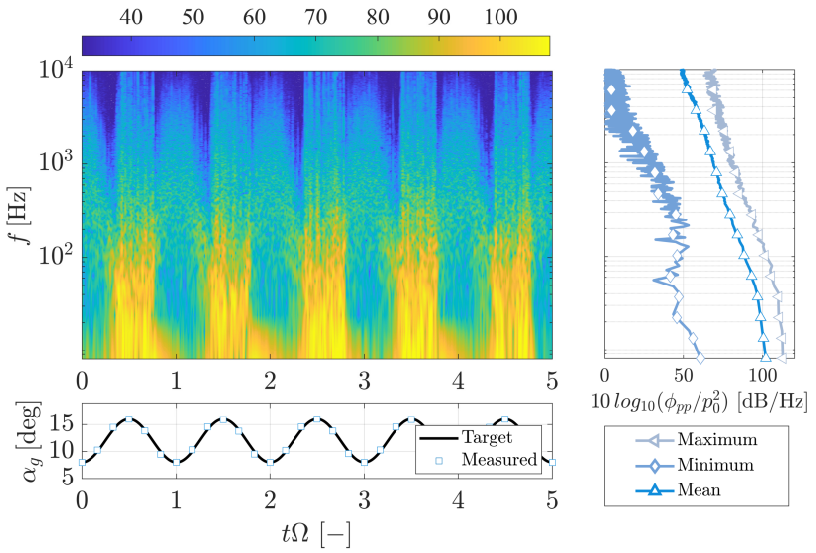

(a)

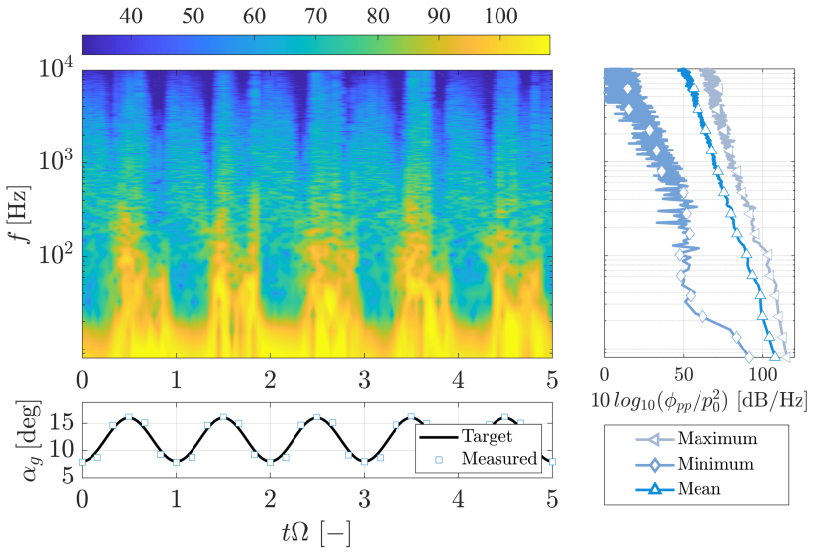

(b)

Figure 11: Surface pressure fluctuation short-time Fourier transform for five oscillation periods at $x/c = 0.90$ for $\alpha_g(t) = 12° + 4° sin(2\pi\Omega t)$: (a) $\Omega = 0.5$ Hz and (b) $\Omega = 2.0$ Hz.

5. Conclusions

The presented work introduced an aeroacoustic test section with tensioned Kevlar windows and the ability to dynamically oscillate a test object by means of a servo motor system. The setup permits near- and far-field aeroacoustic and aerodynamic investigations. Also, the transmission loss due to the presence of the tensioned Kevlar cloth was found to agree well with existing literature [39]. For a statically fixed airfoil

it was shown that it is possible to correct the geometric angle of attack to a free air angle of attack and that blockage corrections are not required until the post-stall regime is reached. Nevertheless, it would be highly beneficial to investigate the unsteady response of Kevlar-walled test sections to pitching airfoils and develop appropriate corrections, if necessary.

Data obtained for a sinusoidally oscillated NACA 0012 airfoil revealed increases in the observed surface pressure spectra levels compared to the surface pressure spectrum observed at the mean angle of attack, both in the pre- and post-stall regimes. For the pre-stall oscillation cases, it was demonstrated that a position weighted averaging results in an accurate prediction of the oscillating airfoil surface pressure spectra. In the case of dynamic stall, a far-field noise increase of several decibel was established for a reduced oscillation frequency of $k_r = 0.094$ in comparison with a reduced oscillation frequency of $k_r = 0.024$. Equally, the surface pressure spectra were found to exceed the spectra of the mean angle of attack substantially and were underpredicted using the weighted average approach, likely because the flow conditions during dynamic stall hysteresis cannot be replicated in fixed airfoil testing. It was concluded that dynamic measurements are necessary if the angle of attack variation induces dynamic stall. This was further confirmed by a short-time Fourier analysis of the surface pressure fluctuations which allowed the low-frequency surface pressure spectrum increase to be linked to the dynamic stall vortex and a delayed flow reattachment due to the pitching movement. The high frequency surface pressure fluctuation increase was also revealed to coincide with the emergence and convection of the dynamic stall vortex.

Declaration of interest

None.

Acknowledgments

The first author would like to acknowledge the financial support through an EPSRC (Engineering and Physical Sciences Research Council) DTP grant and all authors acknowledge the support of EPSRC via Grant No. EP/R010846/1 "*Effect of Separation and Stall on Aerofoil Noise*".

References

[1] Y. D. Mayer, B. Zang, M. Azarpeyvand, Design of a Kevlar-Walled Test Section with Dynamic Turntable and Aeroacoustic Investigation of an Oscillating Airfoil, in: 25th AIAA/CEAS Aeroacoustics Conference, Delft, The Netherlands, 2019. doi:10.2514/6.2019-2464.

[2] World Health Organization Regional Office for Europe, Environmental Noise Guidelines for the European Region, Technical Report, Copenhagen, Denmark, 2018.

[3] L. D. Knopper, C. A. Ollson, Health effects and wind turbines: A review of the literature, Environmental Health 10 (2011) 78–88. doi:10.1186/1476-069X-10-78.

[4] S. A. S. Ali, M. Azarpeyvand, M. Szőke, C. R. I. Da Silva, Boundary layer flow interaction with a permeable wall, Physics of Fluids 30 (2018). doi:10.1063/1.5043276.

[5] T. Geyer, E. Sarradj, C. Fritzsche, Measurement of the noise generation at the trailing edge of porous airfoils, Experiments in Fluids 48 (2010) 291–308. doi:10.1007/s00348-009-0739-x.

[6] A. Wolf, T. Lutz, W. Wuerz, E. Kraemer, O. Stalnov, A. Seifert, Trailing edge noise reduction of wind turbine blades by active flow control, Wind Energy 18 (2015) 909–923. doi:10.1002/we.1737.

[7] M. Herr, W. Dobrzynski, Experimental Investigations in Low-Noise Trailing-Edge Design, AIAA Journal 46 (2005) 1167–1175. doi:10.2514/1.11101.

[8] B. Lyu, M. Azarpeyvand, S. Sinayoko, Prediction of noise from serrated trailing edges, Journal of Fluid Mechanics 793 (2016) 556–588. doi:10.1017/jfm.2016.132.

[9] Y. D. Mayer, B. Lyu, H. K. Jawahar, M. Azarpeyvand, A semi-analytical noise prediction model for airfoils with serrated trailing edges, Renewable Energy 143 (2019) 679–691. doi:10.1016/j.renene.2019.04.132.

[10] M. Szőke, D. Fiscaletti, M. Azerpeyvand, Effect of inclined transverse jets on trailing- edge noise generation, Physics of Fluids 30 (2018). doi:10.1063/1.5044380.

[11] W. J. McCroskey, The Phenomenon of Dynamic Stall, Technical Report, Ames Research Center, Moffett Field, California, United States, 1981. doi:10.1080/6008555886.

[12] M. Smith, A. Bullmore, M. Cand, R. Davis, Mechanisms of amplitude modulation in wind turbine noise, in: Proceedings of Acoustics 2012, Nantes, France, 2012, pp. 823–828.

[13] S. Oerlemans, An explanation for enhanced amplitude modulation of wind turbine noise, Technical Report NLR-CR-2011-071, National Aerospace Laboratory, Amsterdam, Netherlands, 2011.

[14] A. Choudhry, J. O. Mo, M. Arjomandi, R. Kelso, Effects of wake interaction on downstream wind turbines, Wind Engineering 38 (2014) 535–547. doi:10.1260/0309-524X.38.5.535.

[15] A. Laratro, M. Arjomandi, R. Kelso, B. Cazzolato, A discussion of wind turbine interaction and stall contributions to wind farm noise, Journal of Wind Engineering and Industrial Aerodynamics 127 (2014) 1–10. URL: http://dx.doi.org/10.1016/j.jweia.2014.01.007. doi:10.1016/j.jweia.2014.01.007.

[16] S. Oerlemans, M. Fisher, T. Maeder, K. Kögler, Reduction of wind turbine noise using optimized airfoils and trailing-eratdge serions, AIAA Journal 47 (2009) 1470–1481. doi:10.2514/1.38888.

[17] B. Zajamsek, C. J. Doolan, D. J. Moreau, J. Fischer, Z. Prime, Experimental investigation of trailing edge noise from stationary and rotating airfoils, The Journal of the Acoustical Society of America 141 (2017) 3291–3301. doi:10.1121/1.4983295.

[18] T. F. Brooks, D. S. Pope, M. A. Marcolini, Airfoil Self-Noise and Prediction, Technical Report, NASA Langley Research Center, Hampton, Virginia, United States, 1989. doi:10.1111/j.1469-7580.2012.01504.x.

[19] K. Mulleners, M. Raffel, The onset of dynamic stall revisited, Experiments in Fluids 52 (2012) 779–793. doi:10.1007/s00348-011-1118-y.

[20] T. C. Corke, F. O. Thomas, Dynamic Stall in Pitching Airfoils: Aerodynamic Damping and Compressibility Effects, Annual Review of Fluid Mechanics 47 (2015) 479–505. doi:10.1146/annurev-fluid-010814-013632.

[21] A. Sharma, M. Visbal, Numerical investigation of the effect of airfoil thickness on onset of dynamic stall, Journal of Fluid Mechanics 870 (2019) 870–900. doi:10.1017/jfm.2019.235.

[22] J. G. Holierhoek, J. B. de Vaal, A. H. van Zuijlen, H. Bijl, Comparing different dynamic stall models, Wind Energy 16 (2016) 139–158. doi:10.1002/we.548.

[23] S. Nagarajan, S. Hahn, S. K. Lele, Prediction of Sound Generated by a Pitching Airfoil: A Comparison of RANS and LES, in: 12th AIAA/CEAS Aeroacoustics Conference (27th AIAA Aeroacoustics Conference), Cambridge, Massachusetts, United States, 2006. doi:10.2514/6.2006-2516.

[24] L. Siegel, K. Ehrenfried, C. Wagner, K. Mulleners, A. Henning, Cross-correlation analysis of synchronized PIV and microphone measurements of an oscillating airfoil, Journal of Visualization 21 (2018) 381–395. doi:10.1007/s12650-018-0473-7.

[25] T. Zhou, Y. Sun, R. Fattah, X. Zhang, X. Huang, An experimental study of trailing edge noise from a pitching airfoil, The Journal of the Acoustical Society of America 145 (2019) 2009–2021. doi:10.1121/1.5094898.

[26] L. Li, P. Liu, H. Guo, Y. Hou, X. Geng, J. Wang, Aeroacoustic measurement of 30P30N high-lift configuration in the test section with Kevlar cloth and perforated plate, Aerospace Science and Technology 70 (2017) 590–599. doi:10.1016/j.ast.2017.08.039.

[27] T. Ito, H. Ura, K. Nakakita, Y. Yokokawa, W. F. Ng, R. A. Burdisso, A. Iwasaki, T. Fujita, N. Ando, N. Shimada, K. Yamamoto, Aerodynamic/Aeroacoustic testing in Anechoic Closed Test Section of Low-speed Wind Tunnels, in: 16th AIAA/CEAS Aeroacoustics Conference, Stockholm, Sweden, 2010. doi:10.2514/6.2010-3750.

[28] Y. D. Mayer, H. Kamliya Jawahar, M. Szőke, S. A. S. Ali, M. Azarpeyvand, Design and Performance of an Aeroacoustic Wind Tunnel Facility at the University of Bristol, Journal of Applied Acoustics 155 (2019) 358–370. doi:10.1016/j.apacoust.2019.06.005.

[29] W. J. McCroskey, The Phenomenon of Dynamic Stall, Technical Report, Aeromechanics Laboratory, AVRADCOM Research and Technology Laboratories, Ames Research Center, Moffett Field, California, United States, 1981. doi:10.1080/6008555886.

[30] H. Streifeneder, Glasfaser-Flugzeug-Service GmbH, 2018. URL: http://www.streifly.de/shopbaender-d.htm.

[31] G. M. Corcos, Resolution of Pressure in Turbulence, The Journal of the Acoustical Society of America 35 (1963) 192–199. doi:10.1121/1.1918431.

[32] P. F. Mish, An experimental investigation of unsteady surface pressure on single and multiple airfoils, Ph.D. thesis, Virginia Polytechnic Institute and State University, Virginia, United States, 2003.

[33] P. Bevington, D. K. Robinson, Data Reduction and Error Analysis for the Physical Sciences, 3rd ed., New York, United

States, 2003.

[34] A. G. Sagrado, Boundary Layer and Trailing Edge Noise Sources, Ph.D. thesis, University of Cambridge, 2007.

[35] S. Kline, F. McClintock, Describing uncertainties in single-sample experiments, Mechanical Engineering 75 (1953) 3–8.

[36] E. Sarradj, G. Herold, A Python framework for microphone array data processing, Applied Acoustics 116 (2017) 50–58. doi:10.1016/j.apacoust.2016.09.015.

[37] R. P. Dougherty, Functional Beamforming, in: 5th Berlin Beamforming Conference, Berlin, Germany, 2014.

[38] S. M. Jaeger, W. C. Horne, C. S. Allen, Effect of Surface Treatment on Array Microphone Self-Noise, in: 6th AIAA/CEAS Aeroacoustics Conference and Exhibit, Laihana, Hawaii, United States, 2000. doi:10.2514/6.2000-1937.

[39] W. J. Devenport, R. A. Burdisso, A. Borgoltz, P. A. Ravetta, M. F. Barone, K. A. Brown, M. A. Morton, The Kevlar-walled anechoic wind tunnel, Journal of Sound and Vibration 332 (2013) 3971–3991. doi:10.1016/j.jsv.2013.02.043.

[40] H. C. Garner, E. W. E. Rogers, W. E. A. Acum, E. C. Maskell, Subsonic wind tunnel wall corrections, Technical Report, Advisory Group for Aerospace Research and Development, AGARDograph 109, Teddington, England, 1966.

[41] W. J. Devenport, R. A. Burdisso, A. Borgoltz, P. Ravetta, M. F. Barone, Aerodynamic and Acoustic Corrections for a Kevlar-Walled Anechoic Wind Tunnel, in: 16th AIAA/CEAS Aeroacoustics Conference (31st AIAA Aeroacoustics Conference), Stockholm, Sweden, 2010. doi:10.2514/6.2010-3749.

[42] M. Drela, XFOIL: An Analysis and Design System for Low Reynolds Number Airfoils, in: Low Reynolds Number Aerodynamics: Proceedings of the Conference Notre Dame, Notre Dame, Indiana, United States, 1989.

[43] R. E. Sheldahl, P. C. Klimas, Aerodynamic Characteristics of Seven Symmetrical Airfoil Sections Through 180-Degree Angle of Attack for Use in Aerodynamic Analysis of Vertical Axis Wind Turbines, Technical Report, Sandia National Laboratories Report SAND80-2114, Albuquerque, New Mexico, United States, 1981. doi:10.2172/6548367.

[44] J. G. Coder, M. D. Maughmer, Comparisons of theoretical methods for predicting airfoil aerodynamic characteristics, Journal of Aircraft 51 (2014) 183–191. doi:10.2514/1.C032232.

[45] T. Theodorsen, General Theory of Aerodynamic Instability and the Mechanism of Flutter, Technical Report, National Advisory Committee for Aeronautics. Langley Aeronautical Laboratory, Langley Field, Virginia, United States, 1949.

[46] T. C. Corke, F. O. Thomas, Dynamic Stall in Pitching Airfoils: Aerodynamic Damping and Compressibility Effects, Annual Review of Fluid Mechanics 47 (2015) 479–505. doi:10.1146/annurev-fluid-010814-013632.

[47] S. Moreau, M. Roger, J. Christophe, Flow Features and Self-Noise of Airfoils Near Stall or in Stall, in: 15th AIAA/CEAS Aeroacoustics Conference (30th AIAA Aeroacoustics Conference), Miami, Florida, United States, 2009. doi:10.2514/6.2009-3198.

[48] A. Laratro, M. Arjomandi, B. Cazzolato, R. Kelso, Self-noise of NACA 0012 and NACA 0021 aerofoils at the onset of stall, International Journal of Aeroacoustics 16 (2017) 181–195. doi:10.1177/1475472X17709929.

[49] R. K. Amiet, Noise due to turbulent flow past a trailing edge, Journal of Sound and Vibration 47 (1976) 387–393. doi:10.1016/0022-460X(76)90948-2.

[50] S. Yarusevych, P. E. Sullivan, J. G. Kawall, On vortex shedding from an airfoil in low-Reynolds-number flows, Journal of Fluid Mechanics 632 (2009) 245–271. doi:10.1017/S0022112009007058.